




RESEARCH ARTICLE | JULY 05 2022


## Characterizing the flow and turbulence structure near the last closed flux surface in L-mode plasmas of ASDEX Upgrade

T. Nishizawa ; P. Manz ; G. Grenfell ; M. Griener ; D. Wendler ; D. Brida ; D. M. Kriete ; R. Dux ; T. Kobayashi ; M. Sasaki ; ASDEX Upgrade Team



*Phys. Plasmas* 29, 072304 (2022)

<https://doi.org/10.1063/5.0098294>



### APL Machine Learning

2023 Papers with Best Practices in Data Sharing and Comprehensive Background

[Read Now](#)



# Characterizing the flow and turbulence structure near the last closed flux surface in L-mode plasmas of ASDEX Upgrade

Cite as: Phys. Plasmas **29**, 072304 (2022); doi: 10.1063/5.0098294

Submitted: 6 May 2022 · Accepted: 15 June 2022 ·

Published Online: 5 July 2022



View Online



Export Citation



CrossMark

T. Nishizawa,<sup>1,2,a)</sup> P. Manz,<sup>2,3</sup> G. Grenfell,<sup>2</sup> M. Griener,<sup>2</sup> D. Wendler,<sup>2,4</sup> D. Brida,<sup>2</sup> D. M. Kriete,<sup>5</sup> R. Dux,<sup>2</sup> T. Kobayashi,<sup>6,7</sup> M. Sasaki,<sup>8</sup> and ASDEX Upgrade Team<sup>b)</sup>

## AFFILIATIONS

<sup>1</sup>Research Institute for Applied Mechanics, Kyushu University, Kasuga 816-8580, Japan

<sup>2</sup>Max-Planck-Institut für Plasmaphysik, Boltzmannstr. 2, 85748 Garching, Germany

<sup>3</sup>Universität Greifswald Felix-Hausdorff-Str. 6, 17489 Greifswald, Germany

<sup>4</sup>Physik-Department E28, Technische Universität München, James-Franck-Str. 1, 85748 Garching, Germany

<sup>5</sup>Auburn University, Auburn, Alabama 36849, USA

<sup>6</sup>National Institute for Fusion Science, National Institutes of Natural Sciences, Toki 509-5292, Japan

<sup>7</sup>SOKENDAI (The Graduate University for Advanced Studies), Toki 509-5292, Japan

<sup>8</sup>College of Industrial Technology Nihon University, Narashino 275-8575, Japan

<sup>a)</sup>Author to whom correspondence should be addressed: [t.nishizawa@riam.kyushu-u.ac.jp](mailto:t.nishizawa@riam.kyushu-u.ac.jp)

<sup>b)</sup>See Meyer *et al.* (2019) (<https://doi.org/10.1088/1741-4326/ab18b8>) for ASDEX Upgrade team.

## ABSTRACT

Since high density operation is advantageous for building an efficient fusion reactor, understanding the density limit in tokamaks has been seen as one of the most important issues. This paper reports a series of measurements around the last-closed flux surface (LCFS) in L-mode plasmas by using a thermal helium beam diagnostic. Fluctuation analysis has been employed to characterize the poloidal flow and the turbulence structure. A reversal of the poloidal flow in the scrape-off layer and concomitant cooling of the outer divertor plasma are observed as the density is raised. While, in the confined region, the change in the density barely affects the poloidal flow, a higher density shifts the fluctuation power spectral densities toward lower frequencies and wave numbers. The eddy tilting of this region is consistent with what is expected from the magnetic shear effect. A radially coherent low frequency mode appears in the case of the highest density investigated in this study ( $\bar{n}_e/n_{e,GW} = 0.51$ ), and higher frequencies near the LCFS are modulated by this mode.

© 2022 Author(s). All article content, except where otherwise noted, is licensed under a Creative Commons Attribution (CC BY) license (<http://creativecommons.org/licenses/by/4.0/>). <https://doi.org/10.1063/5.0098294>

## I. INTRODUCTION

Understanding the operational limits of tokamaks is essential to develop a safe and efficient scenario for a fusion reactor. One of those limitations is the density limit. In most cases, tokamak plasmas cannot be sustained above the Greenwald density  $\bar{n}_G(10^{20} \text{ m}^{-3}) = I_p \text{ (MA)} / \pi a^2 \text{ (m}^2)$ ,<sup>1,2</sup> where  $\bar{n}_G$  is the line-averaged density,  $I_p$  is the plasma current, and  $a$  is the minor radius. While the Greenwald formula is largely successful, there are a few examples where densities exceeding the Greenwald limit are achieved,<sup>3,4</sup> and others where the plasma is lost before the Greenwald limit is reached.<sup>5</sup> In order to establish a reliable high density operation, it is necessary to reveal the underlying mechanisms that govern the density limit.

Since the early days, it has been known that radiative cooling can lead to a disruption.<sup>2,6</sup> References 7 and 8 introduced the thermo-resistive effect to describe how the radiated power increases. It was shown that current density perturbations caused by the local radiative cooling in the edge can create magnetic islands, leading to the loss of confinement. This process further enhances the radiated power since main ions and impurities tend to radiate more efficiently at lower temperatures. In this model, the linear dependence on  $I_p$ , which is the same as the Greenwald limit, can be recovered for a local density limit. In addition, the existence of magnetic islands prior to a disruption was experimentally verified while a helical impurity radiation pattern, which should cause current density perturbations, was not identified.<sup>9</sup>

Even though radiative cooling is likely to trigger a disruption in the end, there still needs to be some mechanism responsible for initial cooling in the edge as the density limit is approached. Reference 10 showed that the electromagnetic effects, which are linked to the radial gradient of poloidal beta  $\beta_p$ , result in a catastrophic increase in transport when finite collisionality prevents the adiabatic response of electrons from providing the sufficient stabilization. In fact, a clear boundary of the experimentally observed L-mode density limits is drawn in the phase space defined by the  $\beta_p$  gradient and collisionality parameters.<sup>5,11–14</sup> The Greenwald-like linear dependence of the critical density on  $I_p$  can also be derived from the condition under which the electromagnetic effects become important for the dominant instability (resistive ballooning mode).<sup>5</sup>

In the low  $\beta$  regime, an electrostatic fluid model (the Hasegawa–Wakatani model) is also capable of reproducing the transport enhancement, which may lead to a disruption.<sup>15</sup> In this case, the transport regulation is lost by the collapse of the zonal flow shear layers as the plasma becomes more collisional, and the adiabatic response is hampered. Indeed, the measurements of edge plasmas showed that the shearing rate of the poloidal flow and the non-linear drive for the low-frequency zonal flows decrease as the collisionality is raised.<sup>16</sup>

The focus of this paper is to shed light on the underlying mechanism of the L-mode density limit in terms of the edge flow profile and the turbulence structure. Similar work based on probe measurements has already been reported in Ref. 17. The present work mainly uses a thermal helium beam diagnostic,<sup>18</sup> which is able to simultaneously measure multiple locations, including both the confined region and the near scrape-off layer (SOL). This diagnostic capability helps highlight new aspects of the physics near the last closed flux surface (LCFS). Among the several proposed forms of the control parameter for collisionality, the turbulence parameter<sup>5,14</sup>  $\alpha_t \propto n_e/T_e^2$  is employed in this paper to characterize the electron response. When  $\alpha_t \ll 1$ , the electron response is close to adiabatic while the hydrodynamic description is valid when  $\alpha_t \gg 1$ . The explicit definition of  $\alpha_t$  is given in Refs. 5 and 14.

This paper is organized as follows: Sec. II discusses the thermal helium beam diagnostic and the use of the He I line intensities. The poloidal flow measurements are provided in Sec. III with the emphasis on the outer divertor condition. Section IV characterizes the turbulence structure inside the LCFS. Conclusions are given in Sec. V.

## II. FLUCTUATION MEASUREMENTS USING A THERMAL HELIUM BEAM DIAGNOSTIC

Figures 1(a) and 1(b) show the observation points of the thermal helium beam diagnostic (THD) at ASDEX-Upgrade (AUG). Active emission of He I lines due to the electron impact excitation is induced by puffing a helium gas from the wall. Helium puffs are modulated at 10 Hz, allowing for the background subtraction. The light collected from the observation points is fed to a polychromator, which simultaneously measures the intensities of 587, 667, 706, and 728 nm He I lines. Each emission line is detected by a photo-multiplier tube, and the signals are recorded at the sampling frequency of 900 kHz. Detailed descriptions on the diagnostic system can be found in Ref. 18. The intensity of a He I line is given by

$$I_\lambda = n_{\text{He}} n_e \text{PEC}_\lambda, \tag{1}$$

where  $\lambda$  is the wavelength of the He I line and  $n_{\text{He}}$ ,  $n_e$ , and  $T_e$  are the neutral helium density, the electron density, and the electron temperature, respectively.  $\text{PEC}_\lambda$  is called a photon emissivity coefficient.

The present work investigates fluctuations around the LCFS. Typical emission intensity profiles of He I lines are shown in Fig. 1(c). Once a cloud of the neutral helium gas encounters a hotter and denser plasma near the confined region,  $n_{\text{He}}$  rapidly decreases due to ionization while enhanced interactions with the plasma lead to more frequent photon emission per single helium atom. As a result of these two effects, the emission intensities of the He I lines peak near the LCFS. Note that  $n_{\text{He}}$  depends on the trajectory the helium atoms take from the gas valve to the observation point. Thus, the fluctuations in  $I_\lambda$  may also contain non-local effects. Reference 19 introduced a technique to remove the  $n_{\text{He}}$  dependence by evaluating the following quantity:

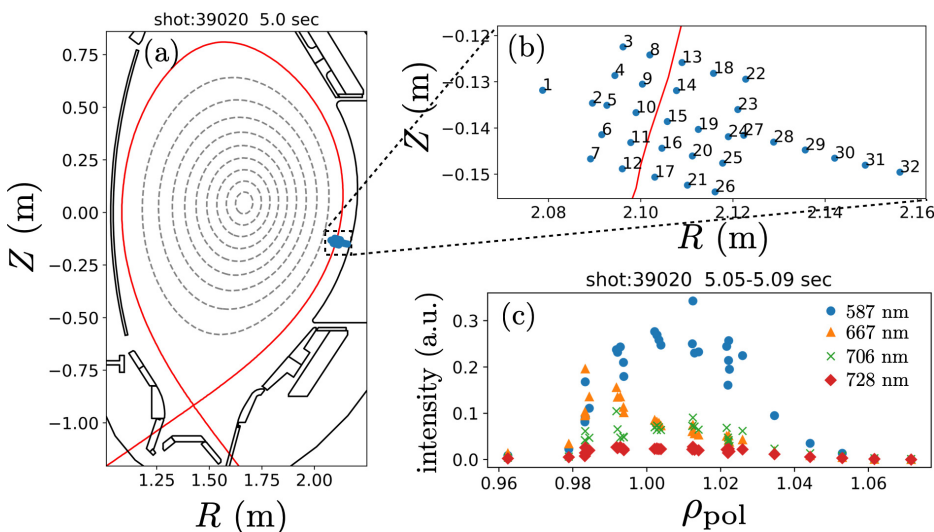


FIG. 1. Magnetic geometry (a) and observation locations of the thermal helium beam diagnostic (b). Typical intensities of the He I lines are shown in (c). The intensities are only relatively calibrated.

$$\begin{aligned}
 R &\equiv \frac{\sum_{i \in B} c_i^B I_{i,0} \sum_{k \in A} c_k^A I_k}{\sum_{j \in A} c_j^A I_{j,0} \sum_{l \in B} c_l^B I_l} \\
 &= \frac{\sum_{i \in B} c_i^B \text{PEC}_{i,0} \sum_{k \in A} c_k^A \text{PEC}_k}{\sum_{j \in A} c_j^A \text{PEC}_{j,0} \sum_{l \in B} c_l^B \text{PEC}_l}, \quad (2)
 \end{aligned}$$

where  $A$  and  $B$  are the groups of He I lines. All four available lines are distributed to either  $A$  or  $B$ . The subscript “ $0$ ” means the time average of the quantity of interest.  $R$  has the sum of He I line intensities in  $A$  for the numerator and in  $B$  for the denominator. Each line intensity is multiplied by a coefficient  $c_X^A$  or  $c_X^B$ . Also,  $R$  is normalized by the averaged values with the subscript “ $0$ .” As can be seen in Eq. (2),  $R$  is independent of  $n_{\text{He}}$ . When the relaxation time between the spin states is neglected, a static collisional radiative model gives  $\text{PEC}_\lambda$  as a function of  $n_e$  and  $T_e$  at the observation point. In such a case,  $R$  can be approximated by a linear function of  $n_e$  and  $T_e$  as follows:

$$R \approx 1 + \alpha_{n_e} \frac{\tilde{n}_e}{n_{e,0}} + \beta_{T_e} \frac{\tilde{T}_e}{T_{e,0}}, \quad (3)$$

where

$$\begin{aligned}
 \alpha_{n_e} &= \frac{n_{e,0}}{\sum_{j \in A} c_j^A \text{PEC}_{j,0}} \sum_{k \in A} c_k^A \left. \frac{\partial \text{PEC}_k}{\partial n_e} \right|_0 \\
 &\quad - \frac{n_{e,0}}{\sum_{i \in B} c_i^B \text{PEC}_{i,0}} \sum_{l \in B} c_l^B \left. \frac{\partial \text{PEC}_l}{\partial n_e} \right|_0, \quad (4)
 \end{aligned}$$

$$\begin{aligned}
 \beta_{T_e} &= \frac{T_{e,0}}{\sum_{j \in A} c_j^A \text{PEC}_{j,0}} \sum_{k \in A} c_k^A \left. \frac{\partial \text{PEC}_k}{\partial T_e} \right|_0 \\
 &\quad - \frac{T_{e,0}}{\sum_{i \in B} c_i^B \text{PEC}_{i,0}} \sum_{l \in B} c_l^B \left. \frac{\partial \text{PEC}_l}{\partial T_e} \right|_0. \quad (5)
 \end{aligned}$$

$\tilde{n}_e$  and  $\tilde{T}_e$  are the fluctuating components of  $n_e$  and  $T_e$ , respectively. The sensitivities to these fluctuations are specified by  $\alpha_{n_e}$  and  $\beta_{T_e}$ . In Secs. III–V, the quantity,

$$\mathcal{R} \equiv R / (\alpha_{n_e} + \beta_{T_e}), \quad (6)$$

is employed for fluctuation measurements. Note that the grouping of  $A$  and  $B$  and the choices of  $c_X^A$  or  $c_X^B$  are arbitrary. These spectral channel groupings and the coefficients are chosen such that a signal-to-noise (S/N) ratio can be maximized in the fluctuation measurements by taking into account  $\alpha_{n_e}$ ,  $\beta_{T_e}$  and the photon noise. The procedure for this optimization is discussed in Ref. 19. In principle, Eqs. (3)–(6) specify the sensitivities to the  $n_e$  and  $T_e$  fluctuations. However, as discussed in Refs. 19–21, experimentally observed He I intensities are not necessarily in complete agreement with collisional radiative models. In addition, the dataset analyzed in this work contains low density cases, for which incomplete equilibration of spin-states may not allow for the adequate use of the static collisional radiative model. Therefore, no quantitative discussion in terms of  $n_e$  and  $T_e$  fluctuations will be made

in this paper.  $n_{e,0}$  and  $T_{e,0}$  are determined by using only three He I lines: 667, 706, and 728 nm, which are most commonly chosen for the THB.<sup>22–24</sup> The intensity of the 587 nm line is rescaled such that its time average becomes the same as the static collisional radiative model calculation for  $n_{e,0}$  and  $T_{e,0}$ .

### III. POLOIDAL FLOWS NEAR THE LAST CLOSED FLUX SURFACE

Poloidal flow ( $V_{\text{pol}}$ ) profiles near the LCFS are investigated by using the time-delay-estimation (TDE) technique.<sup>25,26</sup> In TDE, the time lag  $\tau_{\text{max}}$  that maximizes the correlation function between two fluctuating time series is first determined. Then, the flow velocity is calculated by  $V = \Delta x / \tau_{\text{max}}$ , where  $\Delta x$  is the separation between the two observation points. As can be seen in Fig. 1(b), there are four or five channels at the same radial location near the LCFS. TDE is applied to all combinations of poloidally adjacent channels, and the poloidal flow is calculated by taking average of the multiple flow measurements. The quantity  $\mathcal{R}$  introduced in Sec. II is used for fluctuating time series, and the overlapping period is set to 284  $\mu\text{s}$  in calculating correlation functions. Note that TDE provides the sum of the  $E \times B$  drift and the turbulence phase velocity, which is not necessarily the same as the  $E \times B$  drift velocity inferred from the radial electric field measurements.<sup>27</sup> The flow measurements by using the velocimetry technique,<sup>28,29</sup> which can provide the time of evolution of the two-dimensional flow fields, was also attempted. However, the relatively low S/N ratios of the fluctuation data and the limited coverage of spatial points did not allow for the robust estimation of the flow structure.

Two discharges, #39020 and #38839 in the ASDEX Upgrade tokamak (AUG) are investigated in the present work. Both of them are L-mode ECRH discharges with  $I_p = 0.8$  MA and  $B_t = 2.5$  T, where  $B_t$  is the toroidal field. They are lower single null (LSN) discharges with the favorable  $\nabla B$  drift direction. The magnetic equilibrium is shown in Fig. 1(a). The external heating is 200 kW for #39020 and 300 kW for #38839. In #39020, the line averaged density  $\bar{n}_e$  is ramped up continuously from  $1.5 \times 10^{19}$  to  $4.0 \times 10^{19} \text{ m}^{-3}$  while #38839 has a quasi-stationary period lasting for around 1.5 s with  $\bar{n}_e = 4.8 \times 10^{19} \text{ m}^{-3}$ . The radial profiles of  $V_{\text{pol}}$ ,  $n_e$ , and  $T_e$  are shown in Fig. 2. Note that when  $\tau_{\text{max}}$  is close to zero,  $|V_{\text{pol}}|$  becomes extremely large, causing spurious points. This poses a problem especially when the poloidal flow fluctuates near zero and changes its sign frequently. In order to reduce the influence of spurious points, the median values are plotted instead of the means for the poloidal flow profiles. The Greenwald fraction  $f_{\text{GW}} \equiv \bar{n}_e / n_{\text{GW}}$  is used in the legend to represent the density. The corresponding collisionality parameter  $\alpha_t$  at the LCFS is shown in Table I. At AUG, the L-mode density limit is typically observed between  $f_{\text{GW}} = 0.51$  and 0.63 when the LSN configuration is used.<sup>5</sup> In the highest density case,  $\alpha_t$  exceeds 1, and the adiabatic response of electrons is expected to be hampered. Table I shows that  $\alpha_t$  increases as  $f_{\text{GW}}$  is raised. Therefore, higher densities always correspond to higher collisionalities in this work. The poloidal flow profiles for  $f_{\text{GW}} = 0.28$  and  $f_{\text{GW}} = 0.35$  look similar. Inside the LCFS,  $V_{\text{pol}}$  is in the electron-diamagnetic drift direction (EDD) while the SOL flow is in the ion-diamagnetic drift direction (IDD). As  $f_{\text{GW}}$  increases,  $V_{\text{pol}}$  in the SOL flips the sign and propagates in the EDD except at  $\rho_{\text{pol}} \sim 1.005$ , where the flow direction becomes the EDD again for  $f_{\text{GW}} = 0.51$ . At the moment, there is no adequate explanation of why the flow direction at  $\rho_{\text{pol}} \sim 1.005$  returns to the IDD. One

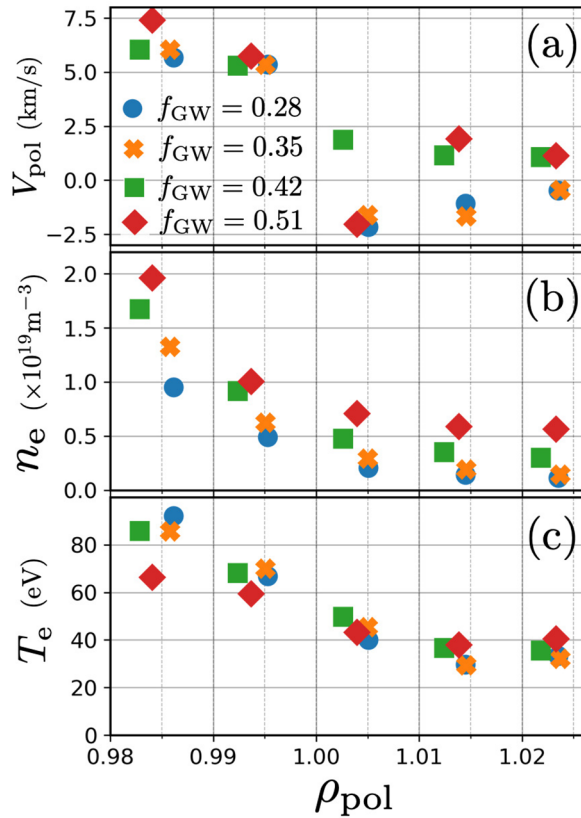


**FIG. 2.** (a) Radial profiles of poloidal flow for different densities calculated by the time-delay-estimation technique.  $V_{\text{pol}} > 0$  corresponds to the flows in the electron diamagnetic drift direction. The data points are the medians of about 200 independent samples. Typical scattering of poloidal flow data can be seen in Fig. 3(a). The radial profiles of electron density and the temperature near the last-closed flux surface are shown in (b) and (c), respectively.  $f_{\text{GW}}$  is the line-averaged density normalized by the Greenwald density limit.

possible candidate is the contribution of blobs, which can propagate in both EDD and IDD.<sup>30,31</sup> It is also important to note that radially propagating tilted structures can also cause a phase lag between poloidally separated channels. More reliable flow measurements are needed for evaluating the flow shear that may play a critical role in the L-mode density limit. In the confined region, the changes in  $V_{\text{pol}}$  are small.

The time evolutions of  $V_{\text{pol}}$  at three different radial locations that cross the LCFS are shown in Fig. 3(a). Also shown are the evolutions of line-integrated density and the profiles of the electron density, the electron temperature, and the ion flux on the outer divertor target. The time window contains  $f_{\text{GW}} = 0.35$  and  $f_{\text{GW}} = 0.42$ , whose  $V_{\text{pol}}$

**TABLE I.** The Greenwald density fractions and the corresponding turbulence parameters<sup>5,14</sup> (measure of collisionality) at the LCFS.

Parameter	Values			
$f_{\text{GW}}$	0.28	0.35	0.42	0.51
$\alpha_t$	0.34	0.45	0.53	1.2

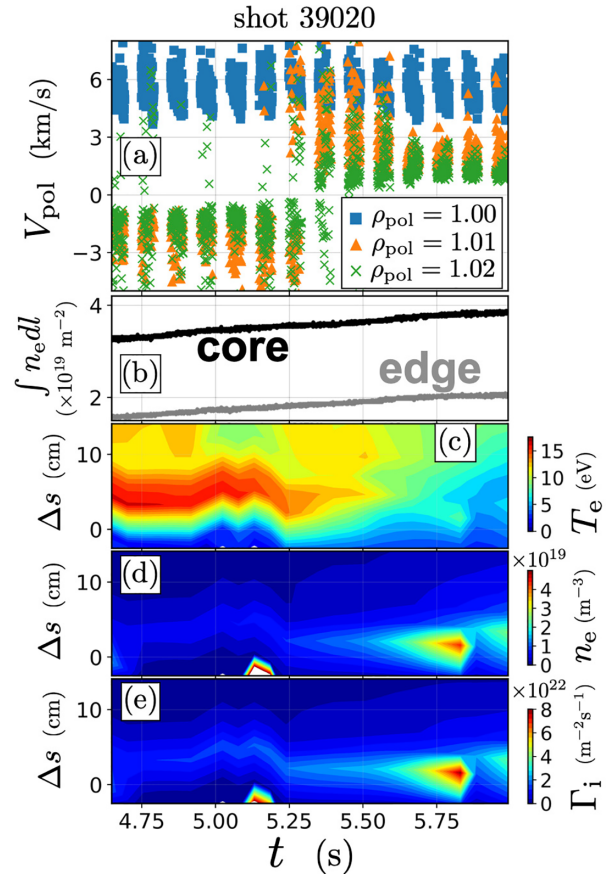


**FIG. 3.** Time evolutions of the turbulent flow velocity at three different radial locations (a), line-integrated electron densities at the core and edge chords (b), the outer-divertor target electron temperature profile (c), the outer-divertor target electron density profile (d), and the ion flux on the outer-divertor target (e). In (c)–(e),  $\Delta s$  is the distance from the strike point. The SOL region is  $\Delta s > 0$ .

profiles are shown in Fig. 2. The flip of the SOL flow direction occurs at round 5.25 s. Around the same time, Figs. 3(c) and 3(d) show that the outer divertor plasma starts to cooldown, and the density there increases. In addition, the ion flux shown in Fig. 3(e) rises, indicating that the outer divertor plasma enters the high-recycling regime. The poloidal flow profiles in L-mode plasmas with different densities were also investigated at HL-2A tokamak by applying TDE to Langmuir probe data.<sup>16</sup> In the HL-2A case,  $|V_{\text{pol}}|$  decreases as  $\bar{n}_e$  increases in the SOL. However, the flow direction remained in the IDD. Another turbulent flow measurement based on the gas-puff-imaging technique at Alcator C-Mod also reported that  $V_{\text{pol}}$  was always in the IDD outside the LCFS when the density was varied.<sup>32</sup> The reversal of  $V_{\text{pol}}$  observed at AUG is likely to be linked to the outer divertor condition.

#### IV. TURBULENCE CHARACTERIZATION IN THE CONFINED REGION

In this section, turbulence characteristics in the confined region are investigated by using frequency analysis. The two brightest He I lines (587 and 667 nm) observed in this measurement have different spin states. The ratio of different spin states tends to be more sensitive

to  $T_e$  than to  $n_e$ . Since  $\mathcal{R}$  used here always has the 587 nm line in the denominator and the 667 nm line in the numerator in Eq. (2), the fluctuation measurements are primarily sensitive to the  $T_e$  fluctuations. The contributions from the  $n_e$  fluctuations may vary for different equilibria and radial locations. However, this effect is neglected in the present work. Figures 4(a)–4(f) show the cross power spectral densities of  $\mathcal{R}$  between two poloidally adjacent channels, the dispersion relations calculated by their cross-phase, and the coherence functions. The channel locations are shown in the insets in Figs. 4(a) and 4(d). For each pair of channels, the spectra are plotted for three different

densities. The similar dispersion relations are obtained for all cases, indicating that the density has a small influence on the turbulent flow velocity as expected from Fig. 2. On the other hand, Fig. 4(a) shows the peak of the cross power spectrum at  $\rho_{\text{pol}} = 0.985$  shifts toward lower frequencies as the density increases. Since the change in the dispersion relation is small, the  $k_{\text{pol}}$  power spectrum is also expected to shift toward lower values. Figure 4(d) shows the cross power spectrum at an outer position  $\rho_{\text{pol}} = 0.995$ . Compared with their counterparts at  $\rho_{\text{pol}} = 0.985$ , the power spectra are concentrated in lower frequency ranges. Given the fact that the dispersion relations are similar between

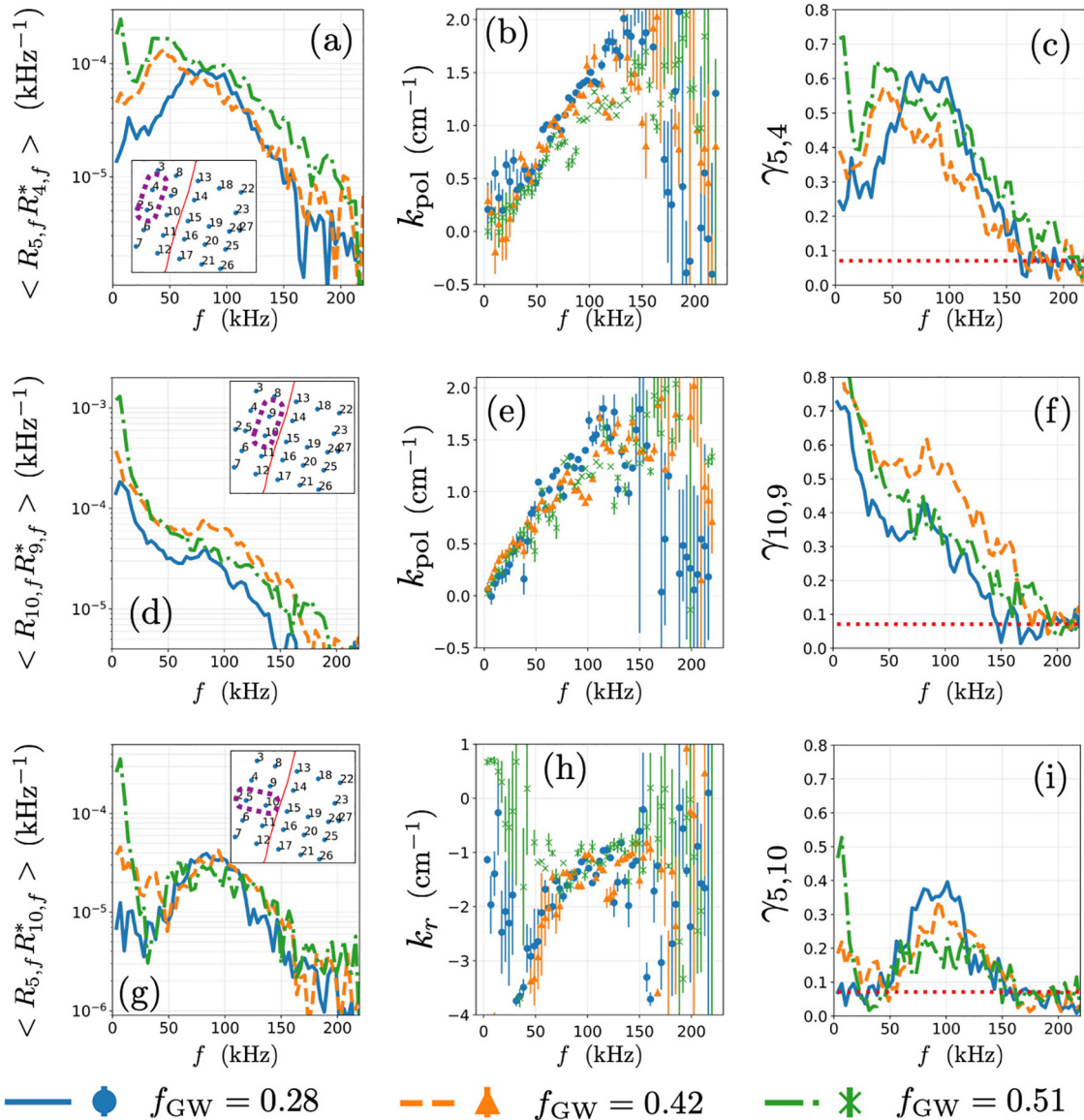


**FIG. 4.** Cross power spectral densities between two poloidally adjacent channels at  $\rho_{\text{pol}} = 0.985$ (a) and  $\rho_{\text{pol}} = 0.995$  (d). Dispersion relations for the poloidal wave number at  $\rho_{\text{pol}} = 0.985$ (b) and  $\rho_{\text{pol}} = 0.995$ (e). Coherence functions at  $\rho_{\text{pol}} = 0.985$ (c) and  $\rho_{\text{pol}} = 0.995$ (f). Also shown are the cross power spectral densities between two radially separated channels (g), the dispersion relation for the radial wave number (h), and the coherence function (i). The channel positions for each case are shown in the insets of (a), (d), or (g). The red dotted lines in (c), (f), and (i) represent the statistical significance levels.

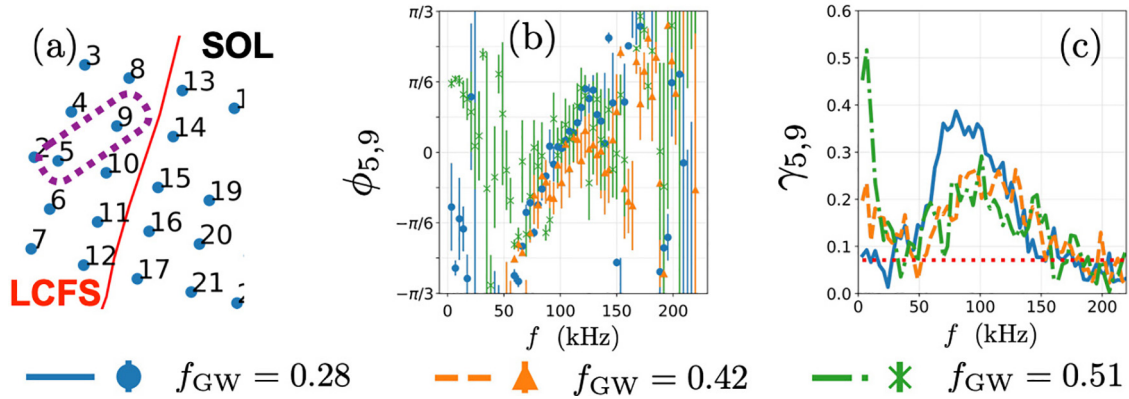


FIG. 5. Locations of the analyzed channels (a), the cross-phase (b), and the coherence function (c). The red dotted line in (c) represents the statistical significance level.

those two radial positions, the turbulence at  $\rho_{\text{pol}} = 0.995$  has larger poloidal structures than at  $\rho_{\text{pol}} = 0.985$ . While, roughly speaking, the cross power spectral density monotonically decays as the frequency increases at  $\rho_{\text{pol}} = 0.995$ , the magnitude of the low frequency components becomes larger as the density increases.

Figure 4(g) shows the cross power spectral densities between two radially separated channels at  $\rho_{\text{pol}} = 0.985$  and  $\rho_{\text{pol}} = 0.995$ , the radial dispersion relations, and the coherence functions. The channel locations are again shown in the inset. Below 50 kHz, the cross power increases as the density becomes higher whereas the cross power stays at similar amplitudes above 50 kHz for all densities. Note that the coherence levels shown in Fig. 4(i) also contribute to the changes in the cross power. Fluctuations below 50 kHz become radially more coherent as the density increases while the opposite trend is observed between 50 and 150 kHz. In this frequency range, the radial wavenumber inferred from the cross phase shown in Fig. 4(h) is negative. This indicates that the outer channel sees the fluctuations before the inner one. However, this relation does not necessarily mean that there exist waves that propagate inward. As discussed in Ref. 33, an inner channel can have a phase lag with respect to an outer channel when

tilted eddies propagate in the poloidal direction. In order to further investigate the fluctuation structure, the cross-phase between both radially and poloidally separated channels is calculated. The positions of the channels, the cross phase between them, and the coherence functions are shown in Fig. 5. The cross phase is close to zero around 100 kHz where the coherence is high. Thus, the channels circled in purple are on the same wave front around 100 kHz. Note that the observation points are below the outer midplane as shown in Fig. 1. At this position, the direction of eddy tilting around 100 kHz is likely to be caused by the magnetic shear as discussed in Refs. 34 and 35. Figure 5 shows that the degree of the eddy tilting has a small, if any, dependence on the density. On the other hand, Ref. 16 reports that the density affects the eddy tilting angle at the outer midplane where the magnetic shear has a small impact on the eddy tilting.

Finally, non-linear coupling is investigated. Figure 6 shows the auto-bicoherence at  $\rho_{\text{pol}} = 0.995$  for different densities. In the lowest density case (a), the frequency components below 50 kHz are coupled to each other. The middle density (b) shows the signs of non-linear interactions also for around 100 kHz. This frequency range is radially coherent as shown in Fig. 4(i). The radial coherence below 25 kHz

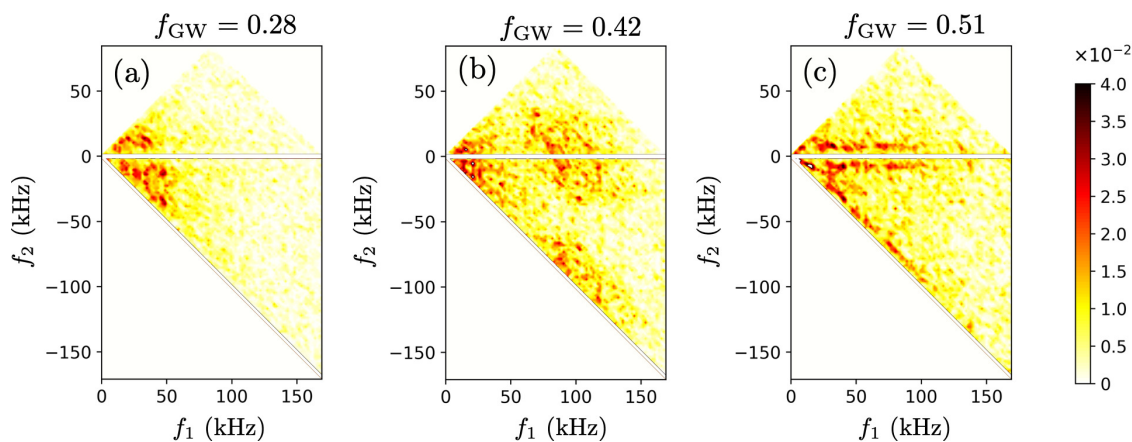


FIG. 6. Auto-bicoherence at  $\rho_{\text{pol}} = 0.995$  for different line-averaged densities. The FFT time window is 568  $\mu\text{s}$ , and each plot has >2000 samples. All spatial channels at the same radial location are utilized to increase the sample size.

16 April 2024 09:48:38

becomes high for the highest density. In this case, frequency components up to 100 kHz are coupled to around 7 kHz. While this bicoherence somewhat resembles the geodesic acoustic modes (GAMs),<sup>16,36,37</sup> no-coherent structure is observed in the power spectral density in Fig. 4(d) even when the frequency resolution is increased. Note that the quantity given in Eq. (6) is primarily sensitive to the  $T_e$  fluctuations while GAMs are most clearly seen in the potential or radial electric field fluctuations near the outer mid-plane. Due to the shift of the cutoff-layer, Doppler reflectometry, which has been used for observing GAMs at AUG,<sup>38</sup> was not available for the confined region when the density was increased. More dedicated measurements are needed in order to identify the type of the low frequency mode. In the case of the similar L-mode study at HL-2A, GAMs were seen inside the LCFS, and their amplitudes increased as the density was raised.<sup>16</sup>

## V. CONCLUSIONS

In order to understand the mechanism underlying the L-mode density limit, the flow and turbulence structure around the LCFS in L-mode plasmas is investigated by using the thermal helium beam diagnostics. The poloidal flow profile measurement based on the time-delay-estimation technique shows that the flow direction changes from the ion-diamagnetic to the electron-diamagnetic drift as the density increases. On the other hand, the variation in the density has a small influence on the poloidal flow in the confined region, and its flow direction stays in the electron-diamagnetic drift direction. The flow direction in the SOL flips in a rather fast timescale (tens of ms) and is accompanied by cooling of the outer-divertor plasma. This change in the flow profile reduces the flow shear and, thus, may lead to an increase in transport. Interestingly, as the density is further raised, the poloidal flow just outside the LCFS becomes in the ion-diamagnetic drift direction again while the poloidal flows at the other radial locations in the near SOL remain in the electron diamagnetic drift direction. Blobs and/or radial flows may contribute to this observation, and further studies are necessary to properly quantify the flow shear in this case.

Fluctuation measurements by using the quantity that is primarily sensitive to the electron temperature have revealed that the power spectral density at  $\rho_{\text{pol}} = 0.985$  shift toward lower frequencies and wavenumbers as the density increases. This change in the spatial scale is in line with the behavior of the resistive ballooning mode, whose characteristic wave-number increases along with the collisionality.<sup>5</sup> The radial correlation between  $\rho_{\text{pol}} = 0.985$  and  $\rho_{\text{pol}} = 0.995$  is high between 50 and 150 kHz. The eddies corresponding to this frequency range are found to be tilted such that the fluctuations in the radially inner positions follow those in the outer positions. This tilt angle is consistent with what is expected of the magnetic shear effects below the outer mid-plane. These observations suggest that the density has a small impact on the degree of tilting around 100 kHz. For the highest density case, bicoherence analysis shows that frequency components up to 100 kHz are modulated by low frequency components around 7 kHz. A high radial coherence is also observed in this low frequency range.

These findings indicate that the divertor condition and the magnetic geometry play non-negligible roles in the edge plasma dynamics. While changes in the spatial structure of turbulence and the non-linear interactions are observed as the density increases, more dedicated studies, such as the local magnetic fluctuation measurements or

the rigorous comparison between instability drives and stabilization due to the flow shear or the diamagnetic effect, are required to reveal the underlying process responsible for the initial edge cooling prior to the radiative collapse in AUG.

## ACKNOWLEDGMENTS

The authors would like to thank Dr. T. Eich, Dr. W. Suttrop, Dr. G. Conway, and Dr. U. Stroth for valuable discussions. This work has been carried out within the framework of the EUROfusion Consortium, funded by the European Union via the Euratom Research and Training Programme (Grant Agreement No. 10105220-EUROfusion). Views and opinions expressed are, however, those of the author(s) only and do not necessarily reflect those of the European Union or the European Commission. Neither the European Union nor the European Commission can be held responsible for them.

## AUTHOR DECLARATIONS

### Conflict of Interest

The authors have no conflicts to disclose.

### Author Contributions

**T. Nishizawa:** Conceptualization (lead); Data curation (lead); Formal analysis (lead); Methodology (lead); Visualization (lead); Writing – original draft (lead); Writing – review and editing (lead). **P. Manz:** Conceptualization (lead); Formal analysis (supporting); Methodology (supporting). **G. Grenfell:** Conceptualization (equal); Data curation (supporting); Formal analysis (supporting); Validation (supporting). **M. Griener:** Data curation (equal); Methodology (equal). **D. Wendler:** Data curation (equal); Methodology (equal). **D. Brida:** Data curation (supporting). **D. M. Kriete:** Formal analysis (supporting); Software (supporting); Writing – review and editing (supporting). **R. Dux:** Funding acquisition (lead); Investigation (supporting). **T. Kobayashi:** Conceptualization (supporting); Formal analysis (supporting); Methodology (supporting). **M. Sasaki:** Conceptualization (supporting); Investigation (supporting). ASDEX Upgrade Team.

## DATA AVAILABILITY

The data that support the findings of this study are available from the corresponding author upon reasonable request.

## REFERENCES

- <sup>1</sup>M. Greenwald, J. Terry, S. Wolfe, S. Ejima, M. Bell, S. Kaye, and G. Neilson, *Nucl. Fusion* **28**, 2199 (1988).
- <sup>2</sup>M. Greenwald, *Plasma Physics Controlled Fusion* **44**, R27 (2002).
- <sup>3</sup>P. Lang, H. Zohm, K. Buchl, J. Fuchs, O. Gehre, O. Gruber, V. Mertens, H. Müller, and J. Neuhauser, *Nucl. Fusion* **36**, 1531 (1996).
- <sup>4</sup>T. H. Osborne, A. W. Leonard, M. A. Mahdavi, M. Chu, M. E. Fenstermacher, R. L. Haye, G. McKee, T. W. Petrie, E. Doyle, G. Staebler, and M. R. Wade, *Phys. Plasmas* **8**, 2017 (2001).
- <sup>5</sup>T. Eich, P. Manz, and ASDEX Upgrade Team, *Nucl. Fusion* **61**, 086017 (2021).
- <sup>6</sup>J. Rapp, P. De Vries, F. Schüller, W. Biel, R. Jaspers, H. Koslowski, A. Krämer-Flecken, A. Kreter, M. Lehnen, A. Pospieszczyk *et al.*, *Nucl. Fusion* **39**, 765 (1999).
- <sup>7</sup>D. A. Gates and L. Delgado-Aparicio, *Phys. Rev. Lett.* **108**, 165004 (2012).
- <sup>8</sup>D. A. Gates, D. P. Brennan, L. Delgado-Aparicio, Q. Teng, and R. B. White, *Phys. Plasmas* **23**, 056113 (2016).



- <sup>9</sup>W. Suttrop, K. Buchl, J. Fuchs, M. Kaufmann, K. Lackner, M. Maraschek, V. Mertens, R. Neu, M. Schittenhelm, M. Sokoll, and H. Zohm, *Nucl. Fusion* **37**, 119 (1997).
- <sup>10</sup>B. N. Rogers and J. F. Drake, *Phys. Rev. Lett.* **79**, 229 (1997).
- <sup>11</sup>B. N. Rogers, J. F. Drake, and A. Zeiler, *Phys. Rev. Lett.* **81**, 4396 (1998).
- <sup>12</sup>B. D. Scott, *Phys. Plasmas* **12**, 062314 (2005).
- <sup>13</sup>B. LaBombard, J. Hughes, D. Mossessian, M. Greenwald, B. Lipschultz, J. Terry, and Alcator C-Mod Team, *Nucl. Fusion* **45**, 1658 (2005).
- <sup>14</sup>T. Eich, P. Manz, R. Goldston, P. Hennequin, P. David, M. Faitsch, B. Kurzan, B. Sieglin, and E. Wolfrum, *Nucl. Fusion* **60**, 056016 (2020).
- <sup>15</sup>R. J. Hajjar, P. H. Diamond, and M. A. Malkov, *Phys. Plasmas* **25**, 062306 (2018).
- <sup>16</sup>R. Hong, G. Tynan, P. Diamond, L. Nie, D. Guo, T. Long, R. Ke, Y. Wu, B. Yuan, and M. Xu, *Nucl. Fusion* **58**, 016041 (2017).
- <sup>17</sup>G. Grenfell, P. Manz, G. D. Conway, T. Eich, J. Adamek, D. Brida, M. Komm, T. Nishizawa, M. Griener, D. Wendler, U. Stroth, and ASDEX Upgrade Team, *Nucl. Fusion 25th International Conference on Plasma Surface Interactions in Controlled Fusion Devices (25th PSI)*.
- <sup>18</sup>M. Griener, E. Wolfrum, M. Cavedon, R. Dux, V. Rohde, M. Sochor, J. M. Muñoz Burgos, O. Schmitz, and U. Stroth, *Rev. Sci. Instrum.* **89**, 10D102 (2018).
- <sup>19</sup>T. Nishizawa, M. Griener, R. Dux, G. Grenfell, D. Wendler, S. Kado, P. Manz, and M. Cavedon, *Rev. Sci. Instrum.* **92**, 103501 (2021).
- <sup>20</sup>M. Griener, J. M. M. Burgos, M. Cavedon, G. Birkenmeier, R. Dux, B. Kurzan, O. Schmitz, B. Sieglin, U. Stroth, E. Viezzer, and E. Wolfrum, *Plasma Phys. Controlled Fusion* **60**, 025008 (2017).
- <sup>21</sup>Y. Iida, S. Kado, and S. Tanaka, *J. Nucl. Mater.* **438**, S1237 (2013), proceedings of the 20th International Conference on Plasma-Surface Interactions in Controlled Fusion Devices.
- <sup>22</sup>T. Barbui, M. Krychowiak, R. König, O. Schmitz, J. M. Muñoz Burgos, B. Schweer, and A. Terra, *Rev. Sci. Instrum.* **87**, 11E554 (2016).
- <sup>23</sup>M. Agostini, P. Scarin, R. Cavazzana, L. Carraro, L. Grando, C. Taliercio, L. Franchin, and A. Tiso, *Rev. Sci. Instrum.* **86**, 123513 (2015).
- <sup>24</sup>J. M. Muñoz Burgos, O. Schmitz, S. D. Loch, and C. P. Ballance, *Phys. Plasmas* **19**, 012501 (2012).
- <sup>25</sup>C. Holland, G. R. Tynan, G. R. McKee, and R. J. Fonck, *Rev. Sci. Instrum.* **75**, 4278 (2004).
- <sup>26</sup>B. Tal, A. Bencze, S. Zoletnik, G. Veres, and G. Por, *Phys. Plasmas* **18**, 122304 (2011).
- <sup>27</sup>M. Xu, G. R. Tynan, P. H. Diamond, P. Manz, C. Holland, N. Fedorczak, S. C. Thakur, J. H. Yu, K. J. Zhao, J. Q. Dong, J. Cheng, W. Y. Hong, L. W. Yan, Q. W. Yang, X. M. Song, Y. Huang, L. Z. Cai, W. L. Zhong, Z. B. Shi, X. T. Ding, X. R. Duan, Y. Liu, and (HL-2A team), *Phys. Rev. Lett.* **108**, 245001 (2012).
- <sup>28</sup>D. M. Kriete, G. R. McKee, R. J. Fonck, D. R. Smith, G. G. Whelan, and Z. Yan, *Rev. Sci. Instrum.* **89**, 10E107 (2018).
- <sup>29</sup>D. M. Kriete, G. R. McKee, L. Schmitz, D. R. Smith, Z. Yan, L. A. Morton, and R. J. Fonck, *Phys. Plasmas* **27**, 062507 (2020).
- <sup>30</sup>B. Nold, G. D. Conway, T. Happel, H. W. Müller, M. Ramisch, V. Rohde, and U. Stroth, *Plasma Phys. Controlled Fusion* **52**, 065005 (2010).
- <sup>31</sup>B. Nold, P. Manz, T. T. Ribeiro, G. Fuchert, G. Birkenmeier, H. W. Müller, M. Ramisch, B. D. Scott, and U. Stroth, *Phys. Plasmas* **21**, 102304 (2014).
- <sup>32</sup>I. Cziegler, J. L. Terry, J. W. Hughes, and B. LaBombard, *Phys. Plasmas* **17**, 056120 (2010).
- <sup>33</sup>N. Fedorczak, P. Manz, S. C. Thakur, M. Xu, G. R. Tynan, G. S. Xu, and S. C. Liu, *Phys. Plasmas* **19**, 122302 (2012).
- <sup>34</sup>N. Fedorczak, P. Diamond, G. Tynan, and P. Manz, *Nucl. Fusion* **52**, 103013 (2012).
- <sup>35</sup>N. Fedorczak, P. Ghendrih, P. Hennequin, G. R. Tynan, P. H. Diamond, and P. Manz, *Plasma Phys. Controlled Fusion* **55**, 124024 (2013).
- <sup>36</sup>K. J. Zhao, T. Lan, J. Q. Dong, L. W. Yan, W. Y. Hong, C. X. Yu, A. D. Liu, J. Qian, J. Cheng, D. L. Yu, Q. W. Yang, X. T. Ding, Y. Liu, and C. H. Pan, *Phys. Rev. Lett.* **96**, 255004 (2006).
- <sup>37</sup>G. Conway, A. Smolyakov, and T. Ido, *Nucl. Fusion* **62**, 013001 (2021).
- <sup>38</sup>G. D. Conway, C. Tröster, B. Scott, and K. Hallatschek, *Plasma Phys. Controlled Fusion* **50**, 055009 (2008).